JGR Oceans

RESEARCH ARTICLE
10.1029/2018JC014299

Key Points:
- Atlantic water transport west and north of Svalbard estimated from sparse VM-ADCP data is 2 Sv in summer
- Yermak Pass Branch was observed in summer and can be as important as the Svalbard Branch for Atlantic water transport
- Atlantic water circulates within Hinlopen trench and strait

Supporting Information:
- Data Set S1

Correspondence to:
S. Menze,
sebastian.menze@hi.no

Citation:
Menze, S., Ingvaldsen, R. B., Haugan, P., Beszczynska-Moeller, A., Fer, I., Sundfjord, A., & Falk-Petersen, S. (2019). Atlantic water pathways along the north-western Svalbard shelf mapped using vessel-mounted current profilers. *Journal of Geophysical Research: Oceans*, *124*, 1699–1716. https://doi.org/10.1029/2018JC014299

Received 23 JUN 2018
Accepted 12 FEB 2019
Accepted article online 28 FEB 2019
Published online 15 MAR 2019
Corrected 11 MAY 2019

This article was corrected on 11 MAY 2019. See the end of the full text for details.

©2019. The Authors.
This is an open access article under the terms of the Creative Commons Attribution-NonCommercial-NoDerivs License, which permits use and distribution in any medium, provided the original work is properly cited, the use is non-commercial and no modifications or adaptations are made.

Atlantic Water Pathways Along the North-Western Svalbard Shelf Mapped Using Vessel-Mounted Current Profilers

Sebastian Menze[1,2], Randi B. Ingvaldsen[1], Peter Haugan[1,2], Ilker Fer[2], Arild Sundfjord[3], Agnieszka Beszczynska-Moeller[4], and Stig Falk-Petersen[5]

[1]Institute of Marine Research, Bergen, Norway, [2]Geophysical Institute, University of Bergen, Bergen, Norway, [3]Norwegian Polar Institute, Tromsø, Norway, [4]Institute of Oceanology, Polish Academy of Sciences, Sopot, Poland, [5]Akvaplan-niva AS, Tromsø, Norway

Abstract A large amount of warm Atlantic water (AW) enters the Arctic as a boundary current through Fram Strait (West Spitsbergen Current [WSC]) and is the major oceanic heat source to the Arctic Ocean. Along the north-western Svalbard shelf, the WSC splits into the shallow Svalbard Branch, the Yermak Branch that follows the slope of the Yermak Plateau, and the Yermak Pass Branch flowing across the plateau. The WSC has previously been studied using moorings, dedicated oceanographic transects, and models. In this study, we mapped the circulation patterns and AW flow around Svalbard using Vessel-Mounted Acoustic Doppler Current Profiler data from multiple surveys during four consecutive summers (2014–2017). Despite the scattered nature of this compiled data set, persistent circulation patterns could be discerned. Spatial interpolation showed a meandering boundary current west of Svalbard and a more homogeneous AW flow, centered around the 1,000-m isobath north of Svalbard. In all summers, we observed a northward jet between 79 and 80°N and the 1,000- and 500-m isobaths, before the WSC divided into the three branches. North of Svalbard, the shallow Svalbard Branch reunited with the Yermak Pass Branch between 10 and 15°E and a part of the AW circulated within Hinlopen Trench. The calculated volume transport of 2 Sv in the upper 500 m compares well with model results and previous observations. Our results further show that the Yermak Pass Branch can be as important as the Svalbard Branch in transporting AW across the Yermak Plateau during summer.

Plain Language Summary We mapped how seawater flows from the Atlantic into the Arctic Ocean around the Svalbard archipelago. To know where and how much water flows from the Atlantic into the Arctic Ocean is important because Atlantic water is the major source of heat, nutrients, and plankton for the Arctic Ocean. Heat from Atlantic water plays a role in the increased melting of sea ice, and the nutrients and plankton drifting with the currents are a major food supply for the Arctic marine ecosystem. We mapped the ocean currents with acoustic current meters that are mounted to research vessels that surveyed the area west and north of the Svalbard archipelago. We found that the Atlantic water flowing around Svalbard can take three different pathways: the shallow Svalbard Branch close to the north-western edge of Svalbard, the Yermak Branch that follows the slope of an underwater plateau north-west of Svalbard, and the Yermak Pass Branch that flows across the plateau and which has not been observed in summer before. We also showed that Atlantic water circulates within Hinlopen trench, a large passage splitting the archipelago, which could create a local ecological hot spot due to the favorable nutrient and plankton supply.

1. Introduction

Atlantic water (AW) flows along the western and northern Svalbard shelf with the West Spitsbergen Current (WSC). This current transports the majority of heat and biological material into the Arctic and has been a focus of oceanographic research since Nansen's expedition in 1893. The circulation patterns around Svalbard have been extensively studied using ocean models, mooring arrays, and oceanographic transects, but an observation-based high-resolution map of AW pathways and large-scale circulation has not been available so far. In this paper, we compiled and analyzed a large data set of acoustic Doppler current profiler observations to study the average circulation patterns.

The Arctic Ocean is connected with the northern Atlantic and Pacific oceans through four main gateways: Fram Strait, the Barents Sea, Bering Strait, and through the Canadian Arctic Archipelago. AW enters the Arctic along two major pathways, the Barents Sea Branch, transporting on average 1.8 Sv (10^6 m^3/s; Skagseth et al., 2008), and the Fram Strait Branch (historically called the WSC), transporting an average 3 Sv of AW (Beszczynska-Moller et al., 2012). The AW passing through the shallow Barents Sea loses substantial amounts of heat before entering the Eurasian Basin (Smedsrud et al., 2013), and the AW passing through Fram Strait, the major deepwater connection of the Arctic to the World Ocean, is the largest heat source for the Arctic Ocean (Rudels et al., 2015). Exchange of water masses and heat has been monitored by regular surveys and a mooring array in Fram Strait since 1997 (Beszczynska-Moller et al., 2012). The WSC is a topographically steered boundary current, which is strongest but also most variable in winter (von Appen et al., 2016). It sheds eddies that facilitate the south-westward recirculation of AW (Hattermann et al., 2016) and AW transport into Nansen Basin (Crews et al., 2018). Along the north-western Svalbard shelf, the WSC splits into the shallow Svalbard Branch (SB), the Yermak Branch that follows the slope of the Yermak Plateau (YB), and the Yermak Pass Branch (YPB) flowing across the plateau (Koenig et al., 2017; Wekerle et al., 2017).

Knowing the circulation patterns and AW pathways around Svalbard is essential to assess the impacts of oceanic heat, volume, salt, and carbon transport on local and pan-Arctic climate. It has been shown that with warming AW inflow, the winter sea ice cover north of Svalbard shrinks and air temperature rises (Ivanov et al., 2012; Onarheim et al., 2014; Piechura & Walczowski, 2009). Recent observations in the Eurasian Basin showed that oceanic heat increasingly contributes to sea ice loss, as AW heat can more easily reach the under-ice boundary layer when stratification weakens and AW shoals (Ivanov et al., 2016; Polyakov et al., 2017).

Understanding the chemical and biological oceanography of the Arctic Ocean is not possible without in-depth understanding of the import and export of water, sea ice, nutrients, carbon, and organisms (Berge et al., 2012; Falk-Petersen et al., 2007; Helland-Hansen & Nansen, 1912). Given the low light and nutrient levels in the Arctic Oceans, the pathways and distribution of advected organisms and nutrients have a strong impact on the ecosystem of the Arctic Basin (Wassmann et al., 2015). The Fram Strait region is of special ecological importance for several reasons: (1) the AW transports large amounts of nutrients, phytoplankton, and zooplankton into the Arctic Ocean and shelf seas (Wassmann et al., 2015); (2) the transpolar ice drift transports sediments, particulate matter, and ice fauna into the Fram Strait that are released during the melting processes (Berge et al., 2012; Proshutinsky et al., 2015); and (3) the increased inflow of AW and declining sea ice has opened up large areas between northern Spitsbergen and Franz Josef Land for new primary production (Falk-Petersen et al., 2014; Onarheim et al., 2014). The declining sea ice and changing oceanographic conditions north and west of Svalbard also affect the migration and distribution of mobile organisms such as marine mammals, fish, and sea birds (Descamps et al., 2016; Falk-Petersen et al., 2014; Haug et al., 2017). Mapping the flow of AW around Svalbard contributes to the baseline knowledge of physical oceanography in the studied region that in turn affects local and pan-Arctic climate and ecosystems.

2. Materials and Methods

The study is based on an observational data set collected using Vessel-Mounted Acoustic Doppler Current Profilers (VM-ADCPs) and Lowered Acoustic Doppler Current Profilers (L-ADCPs) during the summer months of four consecutive years (2014–2017). The surveys covered the Svalbard Shelf and the southern Yermak Plateau and are described in the following section.

2.1. Surveys

Our data set comprises of 10 surveys with RV Helmer Hanssen, RV Håkon Mosby, and RV Oceania in June–September 2014 to 2017. Other research vessels entered the study area during our study period, but we limited our analysis to 10 surveys due to varying VM-ADCP data availability and quality. The survey tracks and stations are displayed in Figure 1, and detailed information about each survey and the instrumentation can be found in Table 1. Four SI_ARCTIC project surveys with RV Helmer Hanssen provided a full data set of VM-ADCP, L-ADCP, and CTD (conductivity, temperature, and depth) data. On these surveys, a vessel-mounted 76.8-kHz RDI Workhorse Mariner ADCP continuously profiled currents in the upper 500 m and was set to record with a vertical bin size of 8 m. We used the software VMDAS (Vessel-

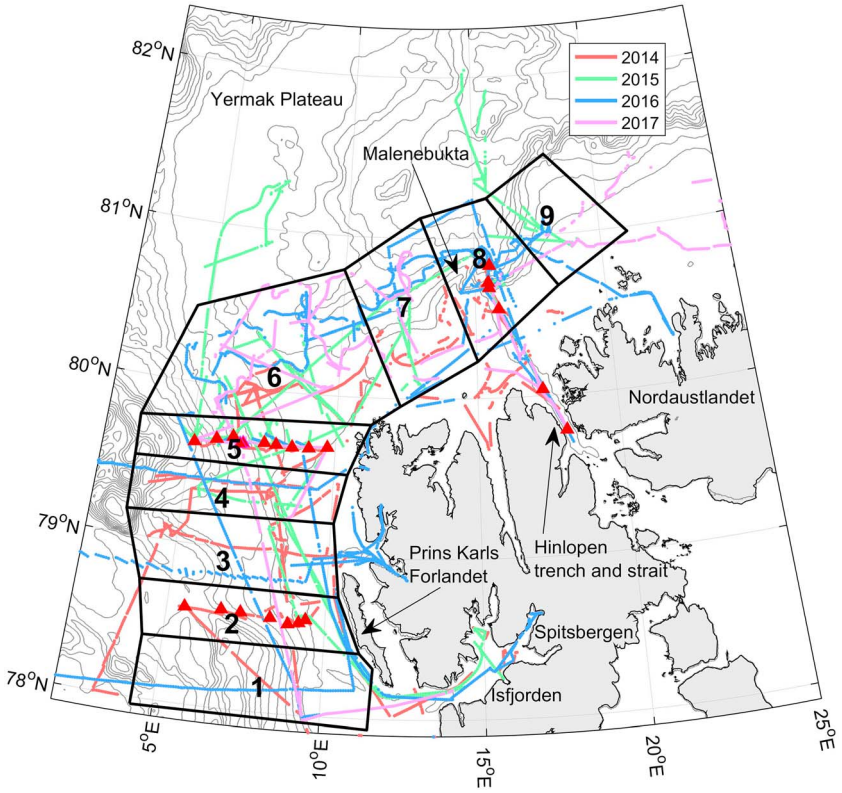

Figure 1. Map of Vessel-Mounted Acoustic Doppler Current Profilers tracks and averaging boxes. The color marks the year of each track: 2014: red; 2015: green; 2016: blue; and 2017: magenta. Bathymetry contours are shown with 200-m intervals (IBCAO; Jakobsson, 2012). The red triangles mark Lowered Acoustic Doppler Current Profiler (L-ADCP) stations. Gaps in the Vessel-Mounted Acoustic Doppler Current Profilers tracks are due to missing or low-quality data.

Table 1
Overview of the Surveys Used to Compile the VM-ADCP Data Set

Date	Survey name/project	Vessel	Data	VM-ADCP frequency	Number of bins	Bin size (m)
20 August to 3 September 2014	SI_ARCTIC	RV Helmer Hanssen	CTD, L-ADCP, VM-ADCP	76.8 kHz	100	8
7 to 17 August 2014	Carbonbridge	RV Helmer Hanssen	VM-ADCP	76.8 kHz	50	8
26 August to 5 September 2014	UNIS AGF214 survey HM2014618	RV Håkon Mosby	VM-ADCP	76.8 kHz	100	8
7 to 14 September 2014	UiB survey HM2014619	RV Håkon Mosby	VM-ADCP	76.8 kHz	100	8
12 to 21 August 2015	UiB survey HM2015617	RV Håkon Mosby	VM-ADCP	76.8 kHz	100	8
19 August to 5 September 2015	SI_ARCTIC	RV Helmer Hanssen	CTD, VM-ADCP	76.8 kHz	100	8
21 August to 1 September 2016	UNIS AB320	RV Helmer Hanssen	VM-ADCP	76.8 kHz	65	8
21 June to 22 July 2016	AREX IOPAN	RV Oceania	VM-ADCP	153.6 kHz	100	8
2 to 16 September 2016	SI_ARCTIC	RV Helmer Hanssen	CTD, L-ADCP, VM-ADCP	76.8 kHz	100	8
21August to 7 September 2017	SI_ARCTIC	RV Helmer Hanssen	CTD, L-ADCP, VM-ADCP	76.8 kHz	100	8

Note. CTD, conductivity, temperature, and depth; L-ADCP, Lowered Acoustic Doppler Current Profiler; VM-ADCP, Vessel-Mounted Acoustic Doppler Current Profilers.

Mounted Data Acquisition System) from RDI instruments to record the VM-ADCP and navigational data. During most of the CTD casts, current profiles were recorded with a downward looking 300-kHz RDI Workhorse Sentinel L-ADCP system using 8-m bins, while temperature and salinity data were collected following standard routines using a 911plus CTD system manufactured by Seabird. In addition to the VM-ADCP data from the four SI_ARCTIC surveys, we used VM-ADCP data from summer time surveys with RV Håkon Mosby, RV Helmer Hanssen, and RV Oceania (instrument frequency and bin size for each cruise are given in Table 1).

2.2. VM-ADCP Postprocessing

The VM-ADCP data were processed with the CODAS processing software package (Hummon, 2016), using 5-min temporal bins and 5-m depth bins. Misalignment of current vectors was removed, and acoustic interference with sea floor, CTD cable, nets, and due to ringing was semiautomatically removed from the data set using the VM-ADCP editing program gautoedit. Automatic thresholding algorithms rejected data with a jitter larger than 0.15 m/s and with a *percentage good* flag lower than 50%. After postprocessing, 49.5% of the bins in the VM-ADCP data set were rejected or missing. To ensure consistency between the surveys, all VM-ADCP profiles were binned vertically in 10-m bins between 10 and 700 m (the first bin centered around 15 m). This data set is available as netcdf file under the following link: https://doi.org/10.21335/NMDC-1323631641.

2.3. L-ADCP Postprocessing

The L-ADCP data were processed using the MATLAB-based inversion software LDEO (Version 4.2; Visbeck, 2002). In the upper layers, VM-ADCP data were used as a constraint for the inversion, whereas bottom echoes were used as a constraint for the lower layers. The average velocity error of the L-ADCP profiles was 0.03 m/s, and the bin size was set to 10 m.

3. Data Analysis

Current measurements obtained with VM-ADCPs (and often also with L-ADCP) vary in both time and space, rendering it a challenging data set to interpret. In this study we used three different approaches to interpret our heterogenous data set: (1) annual binning in polygonal boxes to compare spatial and temporal variability, (2) spatial interpolation to map persistent circulation patterns (objective mapping [OM] and radial basis functions), and (3) discussion of individual L-ADCP sections.

For both the VM-ADCP and L-ADCP current profiles, the along- and across-slope current components were calculated by rotating the current vectors according to the slope aspect in their respective locations. Slope aspect was calculated from the IBCAO bathymetry (Jakobsson et al., 2012), which was smoothed beforehand with a 2-D low-pass filter set to 18-km length. All analyses described here were done in MATLAB 2016a. The corresponding code and a tutorial can be found in this GitHub repository: https://github.com/sebastian-menze/Processing-and-analysis-of-large-ADCP-datasets.

3.1. Detiding Using the AOTIM Tidal Model

Tidal currents inferred from the AOTIM-5 tidal model (Padman & Erofeeva, 2004) were subtracted from the VM-ADCP and L-ADCP data sets. Tides on the shelf surrounding Svalbard can be as strong as 30 cm/s. The AOTIM-5 model has a 5-km resolution and provides estimates for the four most energetic tidal components in the Arctic: M_2, S_2, K_1, and O_1. AOTIM-5 is frequently used to detide ocean velocity data in the Arctic and has provided reliable estimates of barotropic tides (Fer et al., 2010; Meyer et al., 2017). Lacking a suitable model, we did not remove baroclinic tides from our data (discussed further in section 5.1).

3.2. Spatial Interpolation

We applied two different interpolation methods to the VM-ADCP data to visualize and map the general circulation patterns and estimate AW transport along the shelf: OM (also often termed objective analysis) and divergence-free radial basis functions (DF-RBFs).

3.2.1. Objective Mapping

We used OM to interpolate scattered VM-ADCP data onto a regular grid of current vectors. The interpolation is based on all available depth-averaged VM-ADCP observations, consisting of 10 surveys in August–September 2014–2017 (Table 1). The interpolation was conducted prior to rotating the current vectors into

along- and across-isobath components, separately interpolating the east and north velocity components. Combining the VM-ADCP data of multiple surveys improves the spatial coverage and smooths out the temporal variability, yielding a pattern more representative of the large-scale mean circulation.

OM (Bretherton et al., 1976) is an interpolation method used to generate a smooth and regular data grid from scattered data points (similar to interpolation techniques such as kriging). During the interpolation, data points are weighed according to a Gaussian function. It is defined by the standard deviation σ, which describes the *similarity radius*, within which the current field is sufficiently autocorrelated, and the interpolation error E, which describes the relative error we allow during the interpolation. Thus, the OM method requires that the semivariance (autocorrelation) function of the data field has a Gaussian shape.

To confirm this and estimate the similarity radius σ of the VM-ADCP data set, we calculated the average cross-semi-variance of the depth-averaged (between 0- and 500-m depth) current vectors u (northward) and v (eastward) for all profiles in the VM-ADCP data set:

$$\gamma_{i,r} = \frac{1}{\sum i \in r} \left(\sum u_i - u_{i \in r}\right)^2 \left(\sum v_i - v_{i \in r}\right)^2,$$

where $\gamma_{i,\,r}$ denotes the cross-semi-variance of the current vector u and v for profile i in the distance bin (radius) r from profile i and $i \in r$ are the indices of all profiles within distance bin r. We then estimated the median variogram that represents the cross-semi-variance of u and v as a function of distance (Figure S1). In addition, we fitted the following Gaussian function to each profile's variogram:

$$\widehat{\gamma}_r = (\gamma_{\max} - \gamma_{\min})\left(1 - e^{-\frac{r^2}{\sigma^2}}\right),$$

where $\widehat{\gamma}_r$ is the fitted cross-semi-variance, $\gamma_{\max}$ and $\gamma_{\min}$ are the maximum and minimum cross-semi-variances, r is the radius, and σ is the standard deviation that describes the similarity radius in which the current vectors are sufficiently correlated. The resulting distribution of standard deviations (similarity radii) is displayed in Figure S1. The median similarity radius is 58 km, and the 10th and 90th percentiles are 20 and 109 km, respectively. We also calculated the spatial autocorrelation of the u and v component separately using Moran's index and found the autocorrelation dropping to zero above 25-km distance (Figure S2). Based on the two measures, we choose to use a standard deviation σ of 25 km and an interpolation error of 0.4 for the OM algorithm.

The interpolated current field's uncertainty is quantified by the error between the interpolated and observed data (Figure S3). We choose to discard bins with a combined error larger than 0.8 and which were covered less than two summers. Due to the scattered nature of the VM-ADCP data set, not all summers and regions were covered equally (Figure S4). The OA interpolation algorithm is not mass and volume conserving and exhibits convergence and divergence zones of $\pm 0.15\ s^{-1}$ (Figure S5).

3.2.2. Interpolation With Divergence Free Radial Basis Functions

The current fields were also interpolated using DF-RBFs (Vennell & Beatson, 2009). The principle behind this method is to approximate the vector field as the sum of a set of 2-D spline functions whose weights determine the u and v vectors and that are centered at a subset of the data points. In contrast to OM, the DF-RBFs interpolate the u and v vector simultaneously and conserve volume and mass flux in the current field. In cases such as ours, where the observed current vectors contain both temporal and spatial variability (are divergent) the DF-RBFs minimize but do not eliminate divergence in the interpolated vector field. DF-RBFs are especially suitable to extract eddies and meanders from scattered current observations (Rogowski et al., 2014). We followed the method of Vennell and Beatson (2009) and added additional coastal constrains to the interpolation that require the streamfunction of the vector field to be constant along the coastline, as suggested by Vennell and Beatson (2006). For each interpolation, we used the depth-averaged and detided VM-ADCP data and 7% of the observation locations as uniformly distributed center locations for the RBFs and additional RBF centers along the IBCAO coastline.

A difference between OM and DF-RBF interpolation is that OM interpolation emphasizes the dominant features in the scattered data set and produces a smooth field, whereas DF-RBFs aim to fit the potentially noisy observations as close as possible and are thus easily confused by noisy observations or temporal variation. Since OM is based on a spatially weighted averaging it can handle *noisy* data from multiple surveys that

contain both spatial and temporal variability well and emphasizes the dominant features in the scattered data set. The resulting field, however, is not volume and mass conserving. Due to the simplicity of the method, eddies and meanders are interpolated correctly only with multiple crossings, whereas DF-RBFs can interpolate eddies and meanders correctly even with a single crossing. Based on this, we used DF-RBF interpolation to reveal details and temporal variability in the horizontal fields within regions and between months, while we used OM to investigate the along-path AW transports.

3.3. Polygonal Boxes

To compare the scattered VM-ADCP data along the shelf break, we averaged the VM-ADCP profiles in nine polygonal boxes with roughly uniform topography, distributed along bottom depth contours. The averaged section in each box covers the upper 700 m of the water column and the slope between the 2,500- and 0-m isobath (with 200-m bin width). The boundaries of all boxes are marked by black lines in Figure 1. The boundaries of each box are listed in Table S1, while Figure S6 shows the average slope profile for each box.

3.4. Transport Estimates

We calculated the net volume transport into the Arctic Ocean from both the detided L-ADCP and detided VM-ADCP data. For the L-ADCP sections, we calculated the net transport through the entire section, the net transport of AW (using $T > 2$ °C; Beszczynska-Moller et al., 2012), and the net transport in the upper 500 m.

We used three different approaches to estimate transport in the upper 500 m from the VM-ADCP data. Each approach uses the OM current field derived from the VM-ADCP data as the focus was on the dominant features of the AW flow and whether this transport decreases northward/northeastward.

The first approach compares transport along isobaths (2,500 to 0 m, 200-m bin width) between the different polygonal boxes (Figure 1). These transport sections were calculated for each box by multiplying the along-slope current (rotated using the local azimuth at each grid point) averaged in each isobath bin by the average cross-sectional area of each isobath bin. Net transport in each box was calculated by summation of the estimated along-slope transports, calculated separately for all isobath bins in the box.

The second approach followed the steps of the first, but instead of rotating the u and v vectors of the objectively mapped data set using local azimuth angles, we used the average azimuth of each box. We thus calculate the poleward transport through each box with respect to each box's orientation.

For the third approach, we calculated transport through a series of transects using the depth-averaged OM current field. Locations of transects in relation to the boxes and the OM data set are illustrated in Figure S7.

4. Results

4.1. Averaged VM-ADCP Sections

Sections of along-slope flow, averaged in the nine boxes, are compared for four consecutive summers in Figure 2. Coverage of the sections varied between the years; however, some persistent flow patterns can be discerned.

The southernmost box, that is, Box 1, contains a strong jet with the current speed up to 0.5 m/s at approximately 78°N, reflecting the WSC core. In 2014 and 2016 the jet, located between the 2,000- and 1,000-m isobaths, was strongly baroclinic (strongest at the surface), whereas in 2017 it was narrower, constant with depth and centered around the 500-m isobath.

Box 2 was covered only sparsely, but the available data do not indicate a strong jet as in Box 1. However, northward flow centered near the 1,000-m isobath was observed in 2014, 2016, and 2017. No data are available near the 1,000-m isobath from 2015.

The current sections in Box 3 (west of Kongsfjorden) show large differences between the years. The patterns indicate two northward flowing cores with a southward flowing recirculation branch between them. Box 4 shows a fast (approximately 30 cm/s) northward flowing jet, observed in 2014–2016. In 2014 and 2016 a surface intensified jet was found between the 1,000- and 5,00-m isobaths in contrast to summer 2015 when three separate northward flowing branches occurred, possibly related to eddies, instabilities, and recirculation.

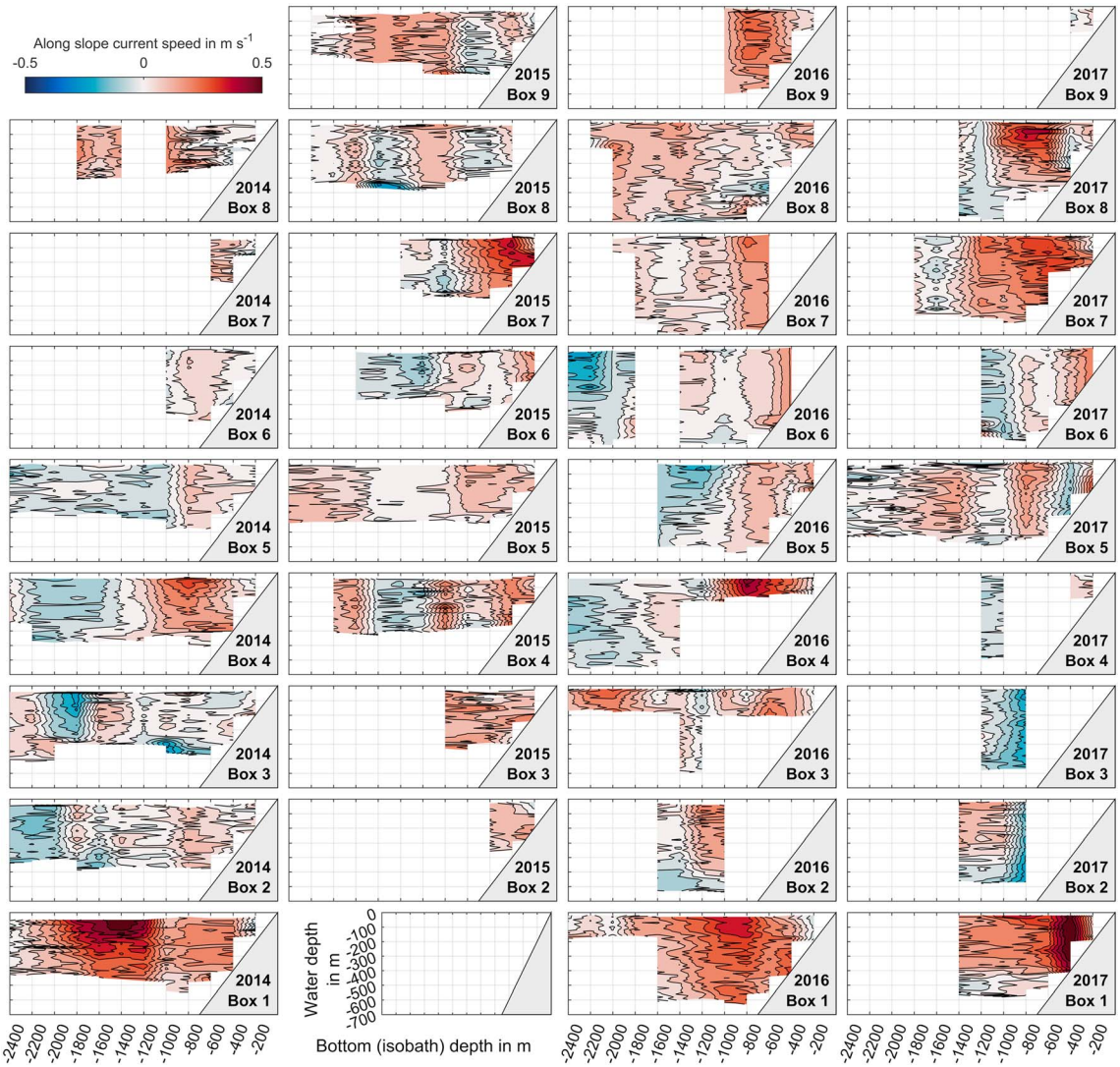

Figure 2. Sections of along-slope currents in a regular isobath coordinate system, averaged within the individual isobath bins for the Boxes 1–9. The red hues mark along-slope flow into the Arctic (north-eastward), while the blue hues indicate the along-slope flow out of the Arctic (to the south-west). Contour lines are drawn every 0.05 m/s, and the color scale ranges from −0.5 to 0.5 m/s. Bottom (isobath) depth is marked as a grey patch.

Box 5 shows a northward surface intensified jet of approximately 20 cm/s between the 1,000- and 500-m isobaths in all years. The jet had a very similar location and strength in all observed years and was the most persistent current in the VM-ADCP data set. West of this jet a recirculation current that varied considerably in width, depth, and strength was observed in all years. In 2015 and 2017 we observed an additional northward current with the highest speeds between 100- and 500-m depth, west of the recirculation current.

Box 6 on the Yermak Plateau was only sparsely sampled, but data from 2015, 2016, and 2017 show that highest northeastern current speeds were found on the shelf above the 500-m isobath. The current sections also indicate southwestward flow offshore of the 1,000-m isobath. A strong barotropic (constant with depth) boundary current was found again in Box 7 with its speed, width, and location varying between years. The current, centered around the 700-m isobath, was fastest (approximately 40 cm/s^{-1}) in 2015 and 2017 and slower (approximately 20 cm/s) in 2016. It was not covered in 2014.

Box 8 displays large interannual variability of the boundary current that is likely related to the irregular bathymetry of the area (Malenebukta canyon). In 2017 a strong surface intensified jet was observed between the 1,000 and 500-m isobaths. Box 9 was only sparsely sampled, but current profiles from 2015 and 2016 indicate a broad boundary current along the slope.

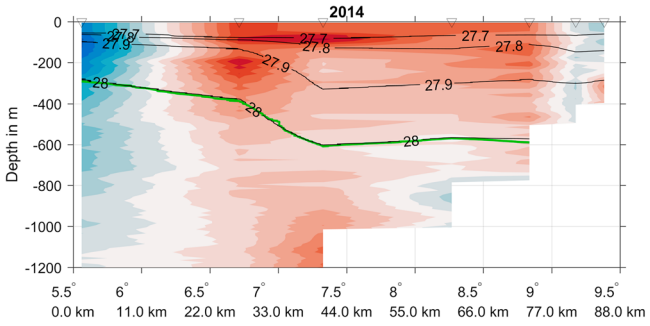

Figure 3. Lowered Acoustic Doppler Current Profiler section along 78.6°N (Box 2). The colored contours show the along-slope current speed ranging from −0.3 to 0.3 m/s^{1} (color scale can be found in Figure 4), the black contours represent potential density ρ_Θ, and the green line depicts the 2 °C isotherm. The triangles mark the locations of stations.

4.2. L-ADCP Sections

The available L-ADCP sections are displayed in Figures 3–5. The L-ADCP section measured in Box 2 in 2014 (Figure 3) agrees well with the averaged VM-ADCP section and shows a wide northward surface intensified boundary current (the WSC) between the 2,000 and 500-m isobaths. A southward recirculating current can be found offshore of the 2,000-m isobath. The L-ADCP sections measured in Box 5 (Figure 4) agree well with the averaged VM-ADCP sections and show a strong and slightly surface intensified boundary current between the 800- and 500-m isobaths in all fully covered sections. Offshore of this flow, a southward recirculating current was observed in 2014. In 2017, only a single station of this transect (marked with a black triangle in Figure 4) was sampled 2 times (23 August and 5 September 2017).

The transect along the Hinlopen trench and across the adjacent shelf showed a similar eastward boundary current centered around the 1,000-m isobath all available years (Figure 5). Unfortunately, no data are available from 2015 and the full width of the boundary current was not sampled. In the Hinlopen trench, the flow was mainly directed along the trench axis that is tilted with a 330° azimuth relative to north. Between 80 and 80.6°N a strong northwestward flow was observed each year with the highest velocity in the upper 100 m. In 2017 we also observed a strong southward current within the Hinlopen strait, south of 80°N.

To compare our L-ADCP and VM-ADCP data to previous studies, we defined AW as water warmer than 2 °C (Beszczynska-Moller et al., 2012). In the L-ADCP sections the lower boundary of AW is indicated by the 2 °C isotherm (green line). West of Svalbard, AW extends to approximately 500-m depth (the AW maximum depth is between 300 and 600 m; Figures 3 and 4), and north of Svalbard the AW layer reaches slightly deeper to approximately 600 m (Figure 5).

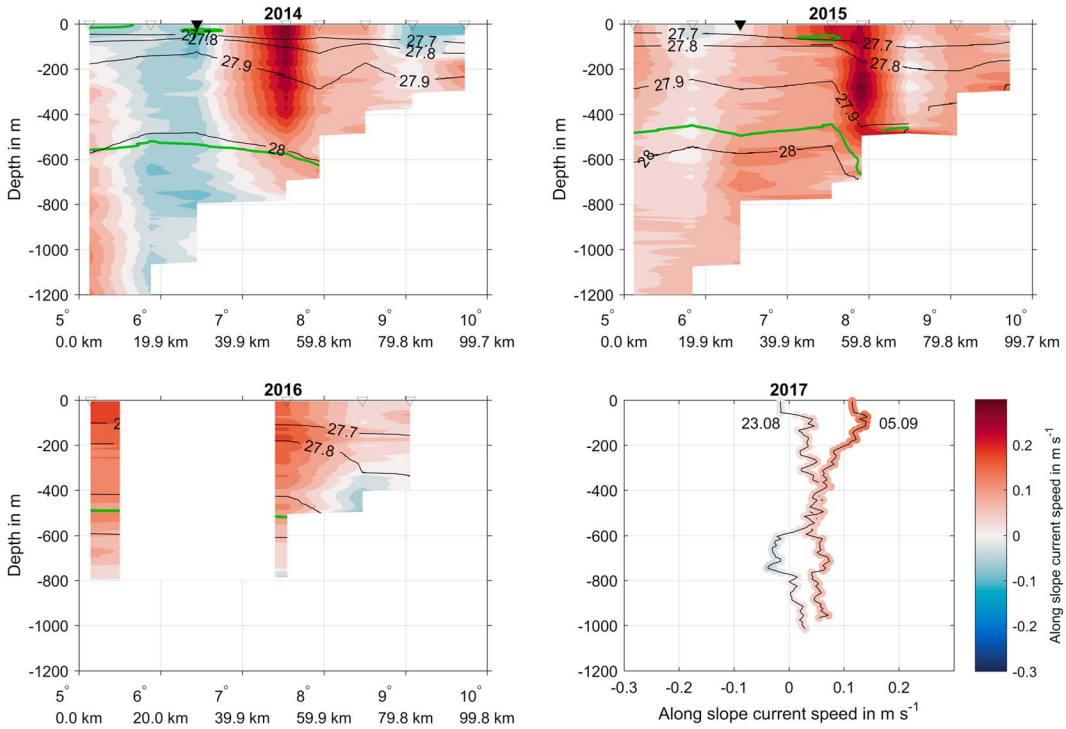

Figure 4. Lowered Acoustic Doppler Current Profiler sections along 79.7°N (Box 5). The colored contours show the along-slope current speed, the black contours represent potential density ρ_Θ, and the green line depicts the 2 °C isotherm. The triangles mark the stations, and the filled black triangles mark the location of the two profiles measured in 2017.

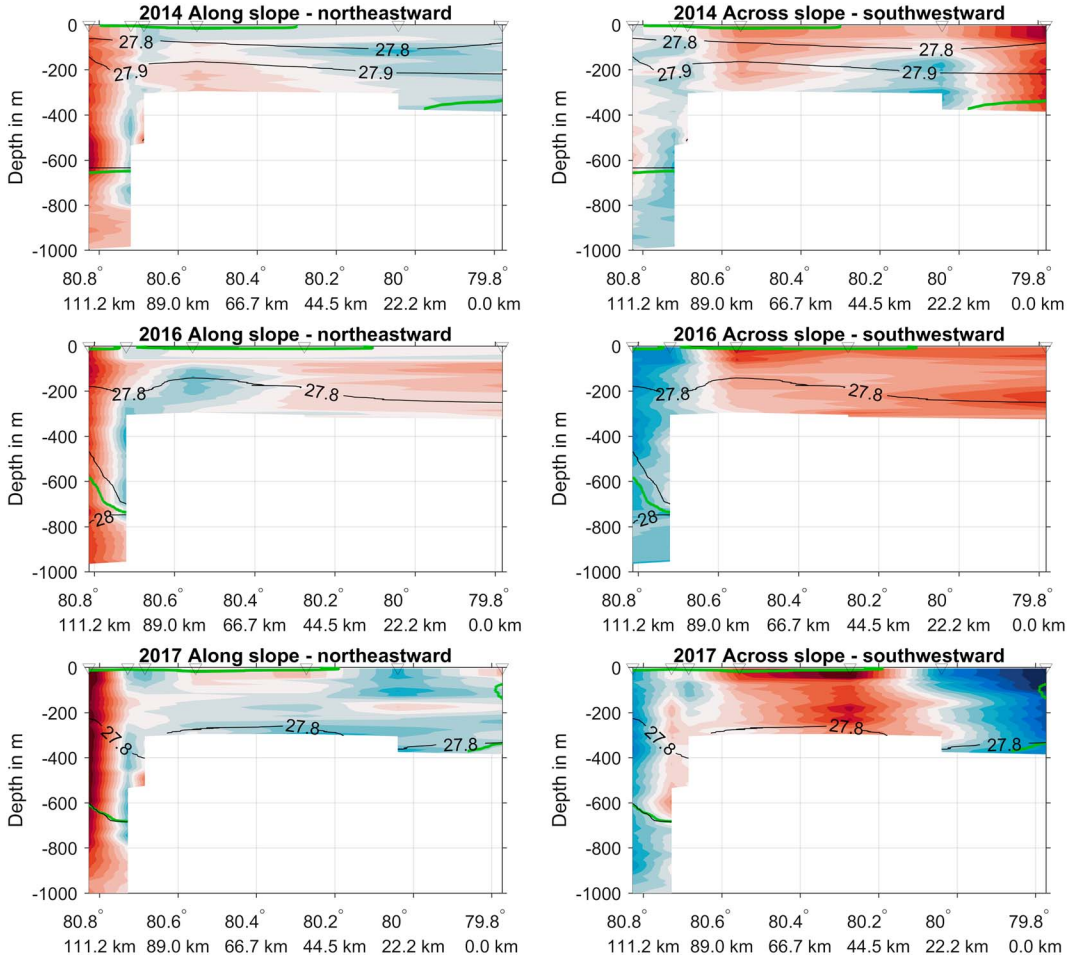

Figure 5. L-ADCP sections along the Hinlopen trench in Box 7 (16°E). The colored contours show the along- and across-slope (shelf break) current speed ranging from −0.3 to 0.3 m/s (color scale can be found in Figure 4), the black contours represent potential density ρ_θ, and the green line the 2 °C isotherm. The triangles mark the stations.

4.3. Depth-Averaged Current Fields

Maps of the depth averaged (20–500 m) VM-ADCP observations and interpolated current fields for different months and years are shown in Figures 6 and 7. Figure 6 focuses on the WSC and Yermak Plateau and Figure 7 on the shelf and trenches north of Svalbard. The AW boundary current is visible as a strong north-eastward flow along the shelf slope to the west and north of Svalbard.

The observed and interpolated circulation patterns show the WSC meandering in relation to the variable slope bathymetry (in August 2014 and 2015; Figures 6a and 6b). The OM interpolation (Figure 6f) shows divergent and convergent patterns west of Svalbard related to eddies and recirculation. The DF-RBF interpolation extracted some of these eddies and meanders successfully, especially in August 2017 on the Yermak Plateau (Figure 6d).

Between 5 and 10°E and 79 and 80°N, the interpolations indicate a persistent northward boundary current toward the Yermak Plateau (Figure 6). The OM implies that this jet splits into three branches: the narrow and shallow SB that follows the 200-m isobath, the YB flowing along the western slope of the Yermak Plateau, and the YPB that branches off the YB toward east at approximately 80.5°N and 6°E and reunites with the SB near 11°E (Figure 6f). Since the OM interpolation is based on the available data at all times, this does not mean that all the three branches are present at all times. The SB was discernible as strong and narrow jet in the observations and DF-RBF interpolations from August 2015, September 2016, and September 2017. The YB was discernible as meandering flow in August 2015,

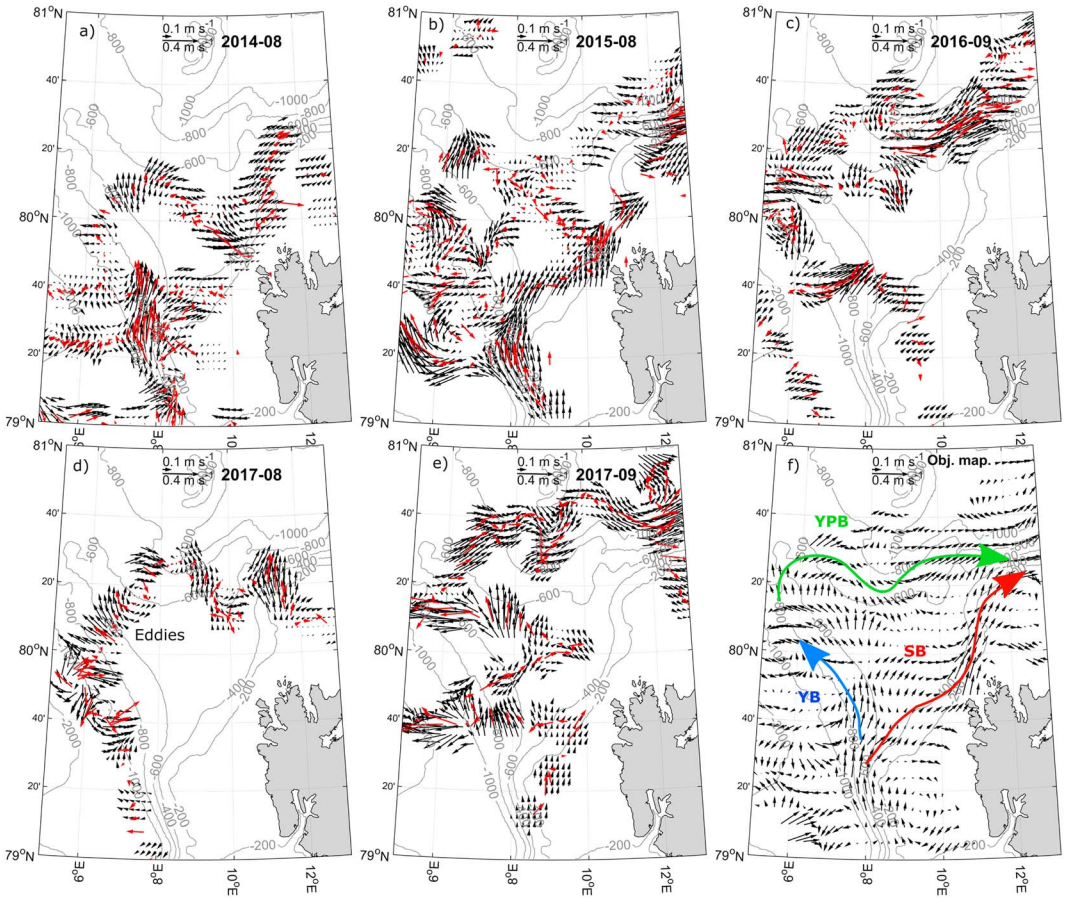

Figure 6. Maps of the observed and interpolated currents on Yermak Plateau. (a–e) The observed currents (red arrows) and divergence-free radial basis function interpolation (black arrows) during months with enough data coverage. Interpolated vectors further than 10 km from the observations are not shown. (f) The objective mapping interpolated current field using all available data. The colored arrows indicate the Atlantic Water branches visible in the objective mapping field and panels a to e: SB, Svalbard Branch (red); YB, Yermak Branch (blue); YPB, Yermak Pass Branch (green).

September 2016, and August and September 2017 and the YPB as meandering flow in September 2016 and 2017.

The OM interpolation suggests that the narrow SB moves toward the shelf around 79.7°N and roughly follows the 400-m isobath north and north-west of Svalbard, whereas the YPB roughly follows the 600-m isobath, and has a much broader and meandering structure. East of 10°E and 80°N the boundary current meanders less and forms a persistent flow that follows the slope (Figure 7). Smaller topographic features such as Malenebukta (north of the Hinlopen trench) seem to have little impact on the large-scale circulation pattern. In the Hinlopen trench, we observed an inflow on the western side and a strong northward outflow on the eastern side.

A map of the OM interpolation error can be found in Figure S3 and shows that the interpolation was least certain (highest interpolation error) in areas with meandering currents west of Svalbard (west of 10°E and south of 79°N), north of 80.5°N on the Yermak Plateau and the sparsely sampled shelf east of 18°E. The boundary current branches between 79°N and Hinlopen Strait are robustly interpolated with significantly less interpolation error.

4.4. Transport Estimates

The three different VM-ADCP-based estimates of the net transport around Svalbard (box average with a local azimuth and a box average azimuth, and transects) are given in Tables S2 and S3. West of Svalbard, we found a northward transport in the upper 500 m ranging between 0.7 and 2.6 Sv for the box method

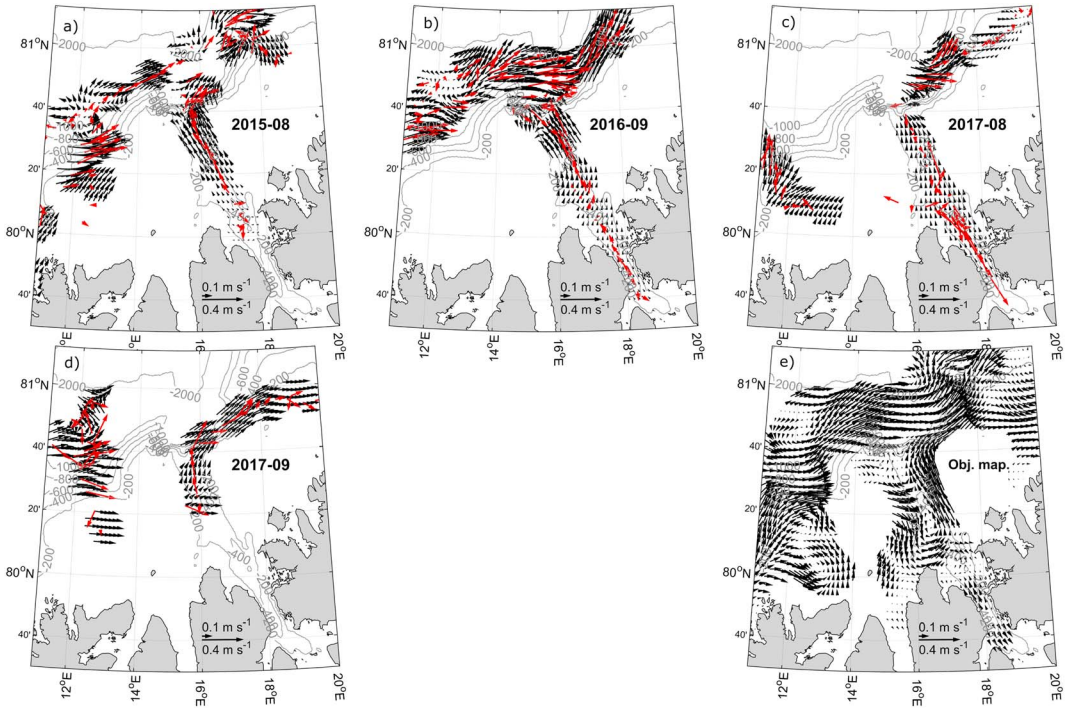

Figure 7. Maps of the observed and interpolated currents north of Spitsbergen. (a–d) The observed currents (red arrows) and divergence-free radial basis function interpolation (black arrow) during month with enough data coverage. Interpolated vectors further than 10 km from the observations are not shown. (e) The objective mapping interpolation using all available data.

and 0.4–4.4 Sv for the transect method; the large range is related to the sparse sampling of the area. Both the box average and transect approach produce a similar transport estimate of about 2 Sv from 79.6°N and poleward (Boxes 4–8, shown in Figure 8). We estimated a transport of 0.8 Sv in the SB and 1.9 Sv in the YPB, based on transects through the interpolated VM-ADCP data set. Because of the uncertainty in the width of the meandering and filamentous YPB, the YPB transport is an order of magnitude estimate and is not as accurate as the SB estimate. The box-averaged transport estimates using the local azimuth (red) are very similar to those using a box-average azimuth (blue).

We also calculated transport from the L-ADCP sections in Boxes 2 and 5 (Table 2). The lateral extent of the L-ADCP section in Box 7 proved too short to obtain reliable transport values. We calculated the total net transport through each section, the net AW transport (water warmer than 2 °C), and net transport in the upper 500 m. The values compare well to the VM-ADCP transport estimates. The AW transport values are similar to the transport in the upper 500 m, because AW was mainly confined to the upper 500 m (Figures 3 and 4).

5. Discussion

The region west and north of the Svalbard archipelago, the northernmost extension of the North Atlantic, is of particular interest with regard to the oceanic heat input to the Arctic Ocean. AW carried northward brings heat, thereby affecting thermal conditions as well as the sea ice cover (e.g., Beszczynska-Möller et al., 2012; Onarheim et al., 2014). The Atlantic current also supplies the region with nutrients and drifting organisms like zooplankton (Basedow et al., 2018; Kosobokova & Hirche, 2009) and micronekton (Knutsen et al., 2017), thereby fueling life north of Svalbard and in the Arctic Ocean (Bluhm et al., 2015; Wassmann et al., 2015). Thus, knowledge about general circulation and transports as well as details of the flow is essential. In this study, we investigated the large-scale AW flow along the western and northern Svalbard shelf break based on a large heterogeneous summer time ADCP data set. We found a persistent boundary current along the shelf slope and a variable offshore flow west of Svalbard, three different AW branches over and around

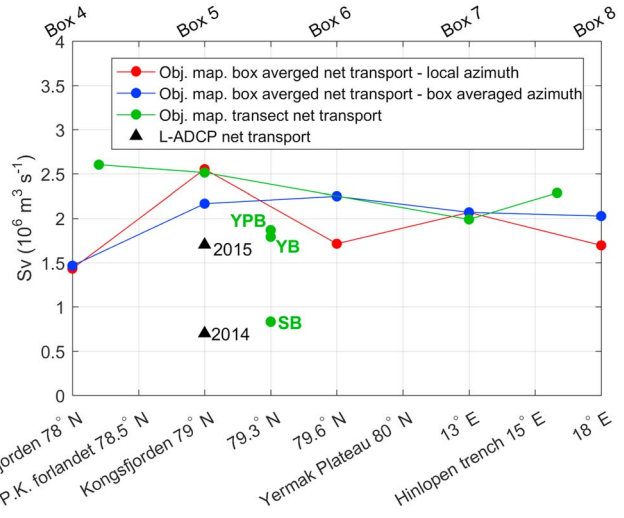

Figure 8. A comparison of net along-slope transport estimates in the upper 500 m around Svalbard: from the Kongsfjord opening to north of Hinlopen trench. The colored lines display transport estimated from the Vessel-Mounted Acoustic Doppler Current Profilers objective mapping data set: blue indicates net along-slope transport calculated by rotating all velocity vectors with the average azimuth of each box, red indicates net along-slope transport calculated by rotating each velocity vector with its local azimuth (slope aspect), and green indicates net along-slope transport calculated through a series of transects (locations displayed in Figure S7). The bold green abbreviations mark the transport estimates for the Yermak Branch (YB), Yermak Pass Branch (YPB), and Svalbard Branch (SB), while the black triangles mark the transport based on the Lowered Acoustic Doppler Current Profiler (L-ADCP) transects.

the Yermak Plateau, and a persistent boundary current along the northern Svalbard shelf slope that is a continuation of the YPB and SB.

5.1. Uncertainty and Limitations

Ocean currents are challenging to measure and interpret, as they vary in both time and space. Common approaches to this problem are limiting the spatial variation by analyzing data from a fixed location (moorings and repeated stations) or limiting the temporal variation by analyzing *snapshots* of the current field (remote sensing and quasi-synoptic transects). In this study, a collection of current measurements that contains both temporal and spatial variability was analyzed with different methods: L-ADCP sections and spatial interpolation to elucidate the spatial variability, and box averaging to analyze the spatiotemporal changes.

How reliable are these methods for separating spatial and temporal variability, and how persistent is the observed circulation system? The box-averaged sections show varying locations and strength of the AW flow each year, but the general flow pattern is similar between the years (Figure 2) and corresponds well with the more sparse L-ADCP sections (Figures 3–5). Although the VM-ADCP data set consists of snapshots of the current field that vary in both space and time, we conclude that careful interpretation of the box averaging and spatial interpolation allows separation of the spatial and temporal variation. However, the objectively mapped areas with sparse data or data from only a single year should be treated with caution, as they might not represent the average circulation pattern accurately. A map of data coverage is shown in Figure S4. Boxes 1, 2, 3, and 9 were sampled less frequently and less uniform than the other boxes, which is reflected in the fluctuating transport estimates for these boxes, that were therefore not shown in Figure 8. We thus focus our discussion and conclusions on the areas with reliable data coverage: Boxes 4–8 and the Hinlopen trench.

The averaging radius used for OM supresses spatial patterns smaller than 25 km and thus effectively filters out eddies that have radii of 5–8 km in the study area (Crews et al., 2018). Also, note that OM is biased to potentially underestimating rather than overestimating current speeds (Thomson & Emery, 2001). In our study area, the growth period for instabilities in summer is approximately 2 days (von Appen et al., 2016). Our L-ADCP sections were measured during 2–3 days and could thus contain variability from current meanders in addition to the observed persistent north-eastward flow.

The AOTIM-5 tidal model is barotropic and cannot represent the baroclinic currents caused by interference effects and internal waves excited by tidal flow. Strong baroclinic tides and internal waves have been shown to occur along the Barents Sea opening, the YB, and the shelf and slopes around Svalbard (Fer et al., 2015; Kurkina & Talipova, 2011; Padman et al., 1992; Skarðhamar et al., 2015). Fer et al. (2015) estimated that around the Yermak Plateau, approximately 50% of the M_2 tidal energy is converted to internal tides that

Table 2
Along-Slope Transport Estimated From the L-ADCP Sections West of Svalbard

	L-ADCP section along 79.7°N - Box 5		L-ADCP section along 78.6°N - Box 2
Year	2014	2015	2014
Net transport in Sv	1.4	2.3	2.3
Net AW (Θ > 2 °C) transport in Sv	0.9	1.7	1.3
Net transport in the upper 500 m in Sv	0.7	1.7	1.2

Note. L-ADCP, Lowered Acoustic Doppler Current Profiler.

are trapped along the topography. As a result, the velocity fields detided using the barotropic tidal model can contain errors. To assess the sensitivity to detiding, we compared the OM interpolation current field based on the VM-ADCP data before and after the removal of tides. The current fields show almost identical patterns (Figures S8 and S9), indicating that the size of the data set and the interpolation scale filter out most tidal currents. The discrepancies between the two current fields are mainly found between 80 and 81°N on the western Yermak Plateau, a region that was only sparsely sampled. Given our focus on the depth-averaged circulation patterns, the SB and YPB, and the limited effect of barotropic tides on our results, we conclude that the AOTIM-5 model removes tidal currents sufficiently well for our purposes.

Since the u and v components of the current fields are interpolated independently during the OM interpolation, the resulting current field is not volume and mass conserving (divergence/convergence displayed in Figure S5). The DF-RBF interpolation, on the other hand, is volume and mass conserving but cannot handle inconsistent data from multiple surveys and gives noisy estimates when too much temporal variation is present in the data set. We used DF-RBFS to interpolate data only from within a month. Figures 6 and 7 compare the circulation fields from the two different interpolation methods and show similar features and circulation patterns. The similarity between OM and monthly DF-RBF current fields, and the consistency of the 2-Sv transport estimates from Boxes 4 to 8, indicates that our findings in Boxes 4–8 and the Hinlopen trench are robust.

5.2. Circulation Patterns and Pathways

The observed current patterns agree well with previous observations and modeling results. Already Helland-Hansen and Nansen (1912) found that a part of the WSC recirculates westward and another part splits into several branches flowing northward and eastward. The presence of the SB and YB has been confirmed frequently since then (Aagaarda et al., 1987), whereas the YPB has been observed and modeled less frequently. It has previously only been observed by acoustically tracked floats (Gascard et al., 1995) and in model simulations (during winter by Hattermann et al., 2016; Koenig et al., 2017; and Crews et al., 2018, and during the entire year by Wekerle et al., 2017). Our observations show that the YPB also exists in summer (Figures 6 and 7). Both the SB and YPB flow over shallow areas with tidal speeds up to 0.2 m/s (Fer et al., 2015; Padman & Erofeeva, 2004), resulting in oscillatory flow patterns and lateral and horizontal mixing.

We found that the circulation patterns from high-resolution models (Hattermann et al., 2016; Koenig et al., 2017; Wekerle et al., 2017) agree well with our observations, especially in pointing out the importance of the YPB for AW transport into the Arctic. The strength and pathways of AW flow around Svalbard are forced by multiple factors: the large-scale oceanic and atmospheric circulation system (Chatterjee et al., 2018; Kawasaki & Hasumi, 2016), the local wind field (Inall et al., 2015), topography, instabilities, and eddies (Hattermann et al., 2016; von Appen et al., 2016; Wekerle et al., 2017). The average large-scale AW flow is confined to slopes, plateaus, and trenches, implying that the bottom topography is a major controlling factor. However, the strength of the three AW branches likely varies with time and season and is related to external forcing such as the strength of the North Atlantic gyres, the wind field, and the instability of the WSC and the rate of eddy formation (Chatterjee et al., 2018; Kawasaki & Hasumi, 2016; Wekerle et al., 2017).

Observations from annual IOPAN summer cruises showed a strong but variable WSC in VM- and L-ADCP measurements between 78 and 79°N and 8 and 12°E, along the shelf break west of Prins-Karls Forland (Walczowski et al., 2005; Walczowski & Piechura, 2006). This agrees with the WSC we observed in the averaged sections (Figure 2) and the objectively mapped data set (Figure 6). In 2003, Walczowski et al. (2005) observed a broad WSC core west of Isfjorden (their section S) between the 1,500- and 200-m isobaths. This concurs with our averaged section in Box 1 that shows a similarly strong along-slope current. Their section Z agrees with our averaged section from Box 2, as both sections show a weaker along-slope current than in Box 1 and some southward flow. Our averaged sections from Box 3 and their section EB agree as well, showing a stronger along-slope northward flow than in Box 2 and a southward flow that varies between the years.

The averaged sections roughly agree with the mooring array and transect observations of Beszczynska-Moller et al. (2012). They observed the WSC core between the 1,200- and 200-m isobaths along the 78.8°N section (west of the northern tip of Prins-Karls Forland). The OM interpolation does not show a strong

northward WSC at this section, but in the areas 50 km south and north of the 78.8°N section. The averaged section in Box 3 (that cover the 78.8°N section) only shows a strong WSC in 2015, and variable currents in 2014 and 2016 (similar to Box 2), whereas Boxes 1 and 4 show a strong boundary current in all sufficiently sampled years. These disparities and discontinuities illustrate the strong temporal and spatial variability of the WSC and can be attributed to undersampling and the scattered nature of our data set. Our snapshot ADCP measurements in Boxes 1 to 3 do most likely not represent the undulating, recirculating, and unstable parts of the WSC reliably. Boxes 4–8 and the Hinlopen trench show better data coverage and correspondingly a more consistent circulation pattern and consistent transport estimates. The discontinuities and divergence in the OM interpolation west of Svalbard (Boxes 1–3) are likely related to eddy activity and recirculation events. The WSC is a highly dynamic current that can be both barotropically and baroclinically unstable (Teigen et al., 2010, 2011; von Appen et al., 2016). Mooring and modeling studies of the WSC and AW currents north of Svalbard agree that largest volume transport and most instabilities occur in winter (Beszczynska-Moller et al., 2012; Koenig et al., 2017; von Appen et al., 2016; Wekerle et al., 2017). Late summer is the period when the WSC is most stable, confirming that our efforts to map the average circulation pattern in the July–September period are purposeful.

North of Svalbard (Figures 6 and 7; north of 80.3°N, and east of 10°E) the SB and YPB join into a persistent boundary current that follows the large-scale features of the shelf slope. Interestingly, the steep canyon-like bathymetry feature termed Malenebukta (80.8°N, 14°E) does not deflect the average boundary current. However, this steep bathymetric structure likely renders the boundary current less stable as the current partly detaches from the slope. The location and strength of the boundary current agree with previous observations farther east and results of model studies (Aksenov et al., 2011; Cokelet et al., 2008; Crews et al., 2018; Pérez-Hernández et al., 2017; Pnyushkov et al., 2015; Vaage et al., 2016; Wekerle et al., 2017). The data coverage is not sufficient to detect whether, and if so where, the YB joins the boundary current.

Our data revealed an inflow of AW on the western side of the Hinlopen trench and outflow on its eastern side. Similar circulation patterns have been found farther east in Kvitøyrenna (Pérez-Hernández et al., 2017) and farther south in Isfjorden (Nilsen et al., 2016). Such circulation is important for bringing warm AW onto the shelf in the deeper trenches. The Hinlopen region is a hot spot for marine mammals (Storrie et al., 2018), which might be linked to the supply of AW facilitating suitable habitat conditions.

5.3. Barotropic and Baroclinic Currents

Analysis of ADCP time series from the mooring array along the 78.8°N (Fram Strait section) showed that the WSC was barotropically unstable during ~40% and baroclinically unstable during ~30% of the measurement record (Teigen et al., 2010, 2011). Further investigations revealed a distinct seasonal cycle in generation of instabilities and eddy kinetic energy: though the WSC is potentially unstable year round, it is most unstable in winter due to reduced stratification and stronger offshore currents related to winter cooling and gyre circulation in the Nordic Seas (von Appen et al., 2016). The eddies formed by the unstable WSC facilitate AW recirculation in Fram Strait (Hattermann et al., 2016) and, beyond the Yermak Plateau, AW transport from the boundary current into the Nansen Basin (Crews et al., 2018).

West of Svalbard, the averaged sections (Figure 2) and L-ADCP profiles (Figures 3 and 4) show a combination of barotropic (constant with depth) and baroclinic currents (surface intensified). The L-ADCP sections at 78.6 and 79.7°N (Figures 3 and 4) show a strong and slightly baroclinic boundary current in the 2 years the section was covered, which agrees well in terms of location and strength with the northward current along the 1,000-m isobath present in the averaged sections in Box 5 (Figure 2). The surface intensified boundary current observed in Box 5 is the most persistent feature in our data set and represents the WSC core before it splits into the three branches. Its persistence compared to other observed currents could be related to local forcing or simply the sparse and irregular sampling in other regions. Due to its baroclinicity (Figure 2), the branching WSC might not be as constrained to follow f/H contours in this area, compared to other slope areas. This could explain why both the SB and YPB can move slightly up-slope on their way across the Yermak Plateau (Figure 6). The combination of a barotropic and baroclinic WSC agrees well with previous studies (Nilsen et al., 2016; von Appen et al., 2016; Walczowski et al., 2005).

Pérez-Hernández et al. (2017) suggest that the boundary current is more barotropic close to the continental slope and more baroclinic (surface intensified) farther offshore as the AW layer expands within the current.

This agrees with the average VM-ADCP sections in Box 1 (Figure 2), where in 2014 and 2016 the boundary current was baroclinic and wide between the 2,000- and 1,000-m isobaths, whereas in 2017 it was barotropic, narrow, and centered at approximately the 500-m isobath.

Here we must note that our VM-ADCP data set mainly covers a depth range between 20 and 500 m; thus, the Polar Surface Water layer (approximately 10–50 m thick) is not properly represented in the VM-ADCP data set. Any shear currents related to the halocline are likely not resolved, since the VM-ADCP data above 20 m are mostly filtered out during postprocessing due to interference and bubble effects.

5.4. Transport

Since 1997 currents in Fram Strait have been monitored along 78.8°N (Box 3) by an array of moored current meters (point and profiling instruments) and CTD sensors (Beszczynska-Moller et al., 2012). Analysis of these data indicates a long-term mean northward AW ($\Theta > 2$ °C) transport of 3.0 Sv through Fram Strait, consisting of a boundary current (termed the WSC core in Beszczynska-Moller et al., 2012) transporting on average 1.8 Sv (1.3 Sv of AW) and a variable offshore current, transporting 2–6 Sv. Whereas the offshore current showed considerable seasonality (strongest in winter), the boundary current (WSC core) manifested little intra-annual and inter-annual variability. For the August–September period, the moorings recorded an average northward AW transport of 2.5 Sv. Beszczynska-Moller et al. (2012) defined AW as water warmer than 2 °C, which approximately covers the upper 500 m of the water column (Figures 3–5) and can thus be compared directly with our transport estimates.

The VM-ADCP data coverage was best in Boxes 4–8, and in Box 5 we estimated an along-slope transport of 1.5 Sv (box-average method) and 2.6 Sv (transect method) in the upper 500 m (Figure 8 and Tables S2 and S3). This compares well with the mooring-based average August–September AW transport estimates from Beszczynska-Moller et al. (2012). Transport estimates from the L-ADCP transects in the same region, on the other hand, gave northward AW transports of 0.9 and 1.7 Sv in 2014 and 2015 respectively (Table 2). Although this is close to the long-term mean of 1.3 Sv for AW slightly further south (Beszczynska-Moller et al., 2012), it is substantially lower than the VM-ADCP data and the August–September average from moorings. It is also somewhat lower than the 2 Sv of northward transport (in the upper 700 m) in the boundary current, and 1–3 Sv in the offshore current, as reported by Basedow et al. (2018) for the region in Boxes 3 and 4 based on L-ADCP data from January, May, and August 2014. Furthermore, is it lower than the AW transport estimates presented by Walczowski et al. (2005) based on L-ADCP data, but this is due to them using a wider definition of AW ($\Theta > 0$ °C instead of $\Theta > 2$ °C). Deviations between the transports based on L-ADCP and VM-ADCP are most likely related to the differences sampling methods (horizontal resolution and temporal average vs. snapshot).

The interannual variation of AW transport west of Svalbard is large. Transport estimates from a model study revealed average AW summer transports west of Svalbard of 2.1 Sv in 2014 and 1.3 Sv in 2015 (Koenig et al., 2017). Even larger differences were evident in our 2014 and 2015 L-ADCP transport estimates in Box 5 (Table 2). These differences illustrate the large variability in the offshore current as well as the considerable current variability due to WSC meanders and eddies (Hattermann et al., 2016; von Appen et al., 2016). Based on this, we find that averaging over all the years 2014–2016 to be the most reliable method for calculating average transports.

North of Svalbard (Boxes 6–8), the OM revealed along-slope transports of 1.7–2.2 Sv in the upper 500 m (Table S3), which is consistent with estimates of the mean AW transport of 2.3 Sv ($\Theta > 1$ °C) measured in the boundary current northeast of Svalbard (at 30°E) by Pérez-Hernández et al. (2017). Our results also show that the YPB, which sheds off the YB at approximately 80.5°N (Figure 7), can be as important as the SB in transporting AW across the Yermak Plateau during summer.

Averaged over all boxes with sufficient data coverage (Boxes 4–8), the most reliable estimate of the August–September AW transport northwest and north of Svalbard is 2 Sv. Recent yearlong mooring observations in the AW boundary current at 31°E show that the current velocity increases significantly over bottom depths of around 800 m—the depth of the Yermak Pass—in fall and winter (Renner et al., 2018). This supports the finding of Koenig et al. (2017) that the YPB is stronger in fall and winter and that this branch provides the overall largest inflow of AW from Fram Strait to the Arctic Ocean.

6. Conclusions

The transport estimates and circulation patterns, obtained from analysis of sparse VM-ADCP data, yield a realistic representation of averaged currents and transports. Collection of current profiling measurements from vessels can thus provide a large potential data source. In our study, we limited the number data sets to the cruises conducted by the authors. A more comprehensive collection using data from all vessels operated in the region merits further analysis. We found an average along-slope transport of 2 Sv of AW northwest and north of Svalbard, which agrees well with literature. The most persistent current pattern found in our study was the boundary current located between 79 and 80°N and between the 1,000- and 400-m isobaths, representing the WSC core. The WSC splits into the YB, YPB and SB, of which the latter two coalesce north of Svalbard and partly follow the trench systems along the shelf. AW enters the Hinlopen trench on the western side and exits on the eastern side, transporting heat and nutrients toward the shelf and strait that could boost local productivity. Based on our observations, we propose that the YPB is comparable to the SB in transporting AW into the Arctic Ocean in summer.

Acknowledgments
We would like to thank the crew and scientists onboard RV Helmer Hanssen, RV Håkon Mosby, and RV Oceania for collecting and sharing ADCP data. We would like to thank the Editor and two anonymous reviewers for helping to improve this manuscript. The ADCP data are available under the following link: https://doi.org/10.21335/NMDC-1323631641. We declare no competing interests. Financial support of the study comes from the Research Council of Norway through the project "The Arctic Ocean Ecosystem" – (SI_ARCTIC, RCN 228896) and from the Institute of Marine Research, Bergen. The work is a contribution to the Barents Sea Ecosystem Programs at Institute of Marine Research, Bergen. Carbonbridge data collection was supported through the Research Council of Norway (RCN 226415).

References

Aagaarda, K., Foldvik, A., & Hillman, S. R. (1987). The West Spitsbergen Current: Disposition and water mass transformation. *Journal of Geophysical Research*, *92*(C4), 3778–3784. https://doi.org/10.1029/JC092iC04p03778

Aksenov, Y., Ivanov, V. V., Nurser, A. J. G., Bacon, S., Polyakov, I. V., Coward, A. C., et al. (2011). The arctic circumpolar boundary current. *Journal of Geophysical Research*, *116*, C09017. https://doi.org/10.1029/2010JC006637

Basedow, S. L., Sundfjord, A., von Appen, W.-J., Halvorsen, E., Kwasniewski, S., & Reigstad, M. (2018). Seasonal variation in transport of zooplankton into the Arctic Basin through the Atlantic gateway, Fram Strait. *Frontiers in Marine Science*, *5*(June), 1–22. https://doi.org/10.3389/fmars.2018.00194

Berge, J., Varpe, Ø., Moline, M. A., Wold, A., Renaud, P. E., Daase, M., & Falk-Petersen, S. (2012). Retention of ice-associated amphipods: Possible consequences for an ice-free Arctic Ocean. *Biology Letters*, *8*(6), 1012–1015. https://doi.org/10.1098/rsbl.2012.0517

Beszczynska-Moller, A., Fahrbach, E., Schauer, U., & Hansen, E. (2012). Variability in Atlantic water temperature and transport at the entrance to the Arctic Ocean, 1997–2010. *ICES Journal of Marine Science*, *69*(5), 852–863. https://doi.org/10.1093/icesjms/fss056

Bretherton, F. P., Davis, R. E., & Fandry, C. B. (1976). A technique for objective analysis and design of oceanographic experiment applied to MODE-73. *Deep Sea Research*, *23*(April 1975), 559–582.

Chatterjee, S., Raj, R. P., Bertino, L., Skagseth, Ø., Ravichandran, M., & Johannessen, O. M. (2018). Role of Greenland Sea gyre circulation on Atlantic water temperature variability in the Fram Strait. *Geophysical Research Letters*, *45*, 8399–8406. https://doi.org/10.1029/2018GL079174

Cokelet, E. D., Tervalon, N., & Bellingham, J. G. (2008). Hydrography of the West Spitsbergen current, Svalbard Branch: Autumn 2001. *Journal of Geophysical Research*, *113*, C01006. https://doi.org/10.1029/2007JC004150

Crews, L., Sundfjord, A., Albretsen, J., & Hattermann, T. (2018). Mesoscale eddy activity and transport in the Atlantic water inflow region north of Svalbard. *Journal of Geophysical Research: Oceans*, *123*, 201–215. https://doi.org/10.1002/2017JC013198

Descamps, S., Aars, J., Fuglei, E., Kovacs, K. M., Lydersen, C., Pavlova, O., et al. (2016). Climate change impacts on wildlife in a High Arctic archipelago - Svalbard, Norway. *Global Change Biology*, (June), 1–13. https://doi.org/10.1111/gcb.13381

Falk-Petersen, S., Pavlov, V., Berge, J., Cottier, F., Kovacs, K. M., & Lydersen, C. (2014). At the rainbow's end: High productivity fueled by winter upwelling along an Arctic shelf. *Polar Biology*, *38*(1), 5–11. https://doi.org/10.1007/s00300-014-1482-1

Falk-Petersen, S., Pavlov, V., Timofeev, S., & Sargent, J. R. (2007). Climate variability and possible effects on arctic food chains: The role of Calanus. In J. B. Ørbæk, R. Kallenborn, I. Tombre, E. N. Hegseth, S. Falk-Petersen, & A. H. Hoel (Eds.), *Arctic Alpine Ecosystems and People in a Changing Environment* (Chap. 9, pp. 147–166). Berlin, Heidelberg: Springer.

Fer, I., Müller, M., & Peterson, A. K. (2015). Tidal forcing, energetics, and mixing near the Yermak Plateau. *Ocean Science*, *11*, 287–304. https://doi.org/10.5194/os-11-287-2015

Fer, I., Skogseth, R., & Geyer, F. (2010). Internal waves and mixing in the marginal ice zone near the Yermak Plateau. *Journal of Physical Oceanography*, *40*(7), 1613–1630. https://doi.org/10.1175/2010JPO4371.1

Gascard, J.-C., Richez, C., & Rouault, C. (1995). New insights on large-scale oceanography in Fram Strait: The West Spitsbergen Current. *Oceanography of the Arctic: Marginal Ice Zones and Continental Shelves*, *49*, 131–182. https://doi.org/10.1029/CE049p0131

Hattermann, T., Isachsen, P. E., von Appen, W.-J., Albretsen, J., & Sundfjord, A. (2016). Eddy-driven recirculation of Atlantic water in Fram Strait. *Geophysical Research Letters*, *43*, 3406–3414. https://doi.org/10.1002/2016GL068323

Haug, T., Bogstad, B., Chierici, M., Gjøsæter, H., Hallfredsson, E. H., Høines, Å. S., et al. (2017). Future harvest of living resources in the Arctic Ocean north of the Nordic and Barents Seas: A review of possibilities and constraints. *Fisheries Research*, *188*, 38–57. https://doi.org/10.1016/j.fishres.2016.12.002

Helland-Hansen, B., & Nansen, F. (1912). The Sea West of Spitsbergen. *Videnskapsselskapets Skrifter. I. Mat.-Naturv. Klasse* 1912, 12.

Hummon, J. (2016). CODAS ADCP processing documentation. Retrieved May 1, 2016, from https://currents.soest.hawaii.edu/docs/adcp_doc/codas_doc/

Inall, M. E., Nilsen, F., Cottier, F. R., & Daae, R. (2015). Shelf/fjord exchange driven by coastal-trapped waves in the Arctic. *Journal of Geophysical Research: Oceans*, *120*, 8283–8303. https://doi.org/10.1002/2015JC011277

Ivanov, V., Alexeev, V., Koldunov, N. V., Repina, I., Sandø, A. B., Smedsrud, L. H., & Smirnov, A. (2016). Arctic Ocean heat impact on regional ice decay: A suggested positive feedback. *Journal of Physical Oceanography*, *46*(5), 1437–1456. https://doi.org/10.1175/JPO-D-15-0144.1

Ivanov, V. V., Alexeev, V. A., Repina, I., Koldunov, N. V., & Smirnov, A. (2012). Tracing Atlantic water signature in the arctic sea ice cover east of Svalbard. *Advances in Meteorology*, *2012*, 1–11. https://doi.org/10.1155/2012/201818

Jakobsson, M., Mayer, L., Coakley, B., Dowdeswell, J. A., Forbes, S., Fridman, B., et al. (2012). The International Bathymetric Chart of the Arctic Ocean (IBCAO) version 3.0. *Geophysical Research Letters*, *39*, L12609. https://doi.org/10.1029/2012GL052219

Kawasaki, T., & Hasumi, H. (2016). The inflow of Atlantic water at the Fram Strait and its interannual variability. *Journal of Geophysical Research: Oceans*, *121*, 502–519. https://doi.org/10.1002/2015JC011375

Knutsen, T., Wiebe, P. H., Gjøsæter, H., Ingvaldsen, R. B., & Lien, G. (2017). High latitude epipelagic and mesopelagic scattering layers—A reference for future Arctic ecosystem change. *Frontiers in Marine Science*, *4*(November). https://doi.org/10.3389/fmars.2017.00334

Koenig, Z., Provost, C., Villacieros-Robineau, N., Sennéchael, N., Meyer, A., Lellouche, J. M., & Garric, G. (2017). Atlantic waters inflow north of Svalbard: Insights from IAOOS observations and Mercator Ocean global operational system during N-ICE2015. *Journal of Geophysical Research: Oceans*, *122*, 1254–1273. https://doi.org/10.1002/2016JC012424

Kosobokova, K., & Hirche, H. J. (2009). Biomass of zooplankton in the eastern Arctic Ocean—A base line study. *Progress in Oceanography*, *82*(4), 265–280. https://doi.org/10.1016/j.pocean.2009.07.006

Kurkina, O. E., & Talipova, T. G. (2011). Huge internal waves in the vicinity of the Spitsbergen Island (Barents Sea). *Natural Hazards and Earth System Sciences*, *11*(3), 981–986. https://doi.org/10.5194/nhess-11-981-2011

Meyer, A., Sundfjord, A., Fer, I., Provost, C., Villacieros Robineau, N., Koenig, Z., et al. (2017). Winter to summer oceanographic observations in the Arctic Ocean north of Svalbard. *Journal of Geophysical Research: Oceans*, *122*, 6218–6237. https://doi.org/10.1002/2016JC012391

Nilsen, F., Skogseth, R., Vaardal-Lunde, J., & Inall, M. (2016). A simple shelf circulation model: Intrusion of Atlantic water on the West Spitsbergen shelf. *Journal of Physical Oceanography*, *46*(4), 1209–1230. https://doi.org/10.1175/JPO-D-15-0058.1

Onarheim, I. H., Smedsrud, L. H., Ingvaldsen, R. B., & Nilsen, F. (2014). Loss of sea ice during winter north of Svalbard. *Tellus Series A: Dynamic Meteorology and Oceanography*, *66*, 1–9. https://doi.org/10.3402/tellusa.v66.23933

Padman, L., & Erofeeva, S. (2004). A barotropic inverse tidal model for the Arctic Ocean. *Geophysical Research Letters*, *31*, L02303. https://doi.org/10.1029/2003GL019003

Padman, L., Plueddemann, A. J., Muench, R. D., & Pinkel, R. (1992). Diurnal tides near the Yermak Plateau. *Journal of Geophysical Research*, *97*(C8), 12,639–12,652. https://doi.org/10.1029/92JC01097

Pérez-Hernández, M. D., Pickart, R. S., Pavlov, V., Våge, K., Ingvaldsen, R., Sundfjord, A., et al. (2017). The Atlantic water boundary current north of Svalbard in late summer. *Journal of Geophysical Research: Oceans*, *119*, 7123–7138. https://doi.org/10.1002/2016JC012486

Piechura, J., & Walczowski, W. (2009). Warming of the West Spitsbergen Current and sea ice north of Svalbard. *Oceanologia*, *51*(2), 147–164. https://doi.org/10.5697/oc.51-2.147

Pnyushkov, A. V., Polyakov, I. V., Ivanov, V. V., Aksenov, Y., Coward, A. C., Janout, M., & Rabe, B. (2015). Structure and variability of the boundary current in the Eurasian Basin of the Arctic Ocean. *Deep-Sea Research Part I: Oceanographic Research Papers*, *101*, 80–97. https://doi.org/10.1016/j.dsr.2015.03.001

Polyakov, I. V., Pnyushkov, A. V., Alkire, M. B., Ashik, I. M., Baumann, T. M., Carmack, E. C., et al. (2017). Greater role for Atlantic inflows on sea-ice loss in the Eurasian Basin of the Arctic Ocean. *Science*, *8204*(April). https://doi.org/10.1126/science.aai8204

Proshutinsky, A., Dukhovskoy, D., Timmermans, M., Krishfield, R., & Bamber, J. L. (2015). Arctic circulation regimes. *Philosophical Transactions of the Royal Society A: Mathematical, Physical and Engineering Sciences*, *373*(2052), 20140160. https://doi.org/10.1098/rsta.2014.0160

Renner, A. H. H., Sundfjord, A., Janout, M. A., Ingvaldsen, R. B., Beszczynska-Möller, A., Pickart, R. S., & Pérez-Hernández, M. D. (2018). Variability and redistribution of heat in the Atlantic water boundary current north of Svalbard. *Journal of Geophysical Research: Oceans*, *123*, 6373–6391. https://doi.org/10.1029/2018JC013814

Rogowski, P., Terrill, E., & Chen, J. (2014). Observations of the frontal region of a buoyant river plume using an autonomous underwater vehicle. *Journal of Geophysical Research: Oceans*, *119*, 7549–7567. https://doi.org/10.1002/2014JC010392

Rudels, B., Korhonen, M., Schauer, U., Pisarev, S., Rabe, B., & Wisotzki, A. (2015). Circulation and transformation of Atlantic water in the Eurasian Basin and the contribution of the Fram Strait inflow branch to the Arctic Ocean heat budget. *Progress in Oceanography*, *132*, 128–152. https://doi.org/10.1016/j.pocean.2014.04.003

Skagseth, Ø., Furevik, T., Ingvaldsen, R., Loeng, H., Mork, K. A., Orvik, K. A., & Ozhigin, V. (2008). Volume and heat transports to the Arctic Ocean via the Norwegian and Barents seas. *Arctic-Subarctic Ocean Fluxes: Defining the Role of the Northern Seas in Climate*, 45–64. https://doi.org/10.1007/978-1-4020-6774-7_3

Skarðhamar, J., Skagseth, Ø., & Albretsen, J. (2015). Diurnal tides on the Barents Sea continental slope. *Deep Sea Research Part I: Oceanographic Research Papers*, *97*, 40–51. https://doi.org/10.1016/j.dsr.2014.11.008

Smedsrud, L. H., Esau, I., Ingvaldsen, R. B., Eldevik, T., Haugan, P. M., Li, C., et al. (2013). The role of the Barents Sea in the Arctic climate system. *Reviews of Geophysics*, *51*, 415–449. https://doi.org/10.1002/rog.20017

Storrie, L., Lydersen, C., Andersen, M., Wynn, R. B., & Kovacs, K. M. (2018). Determining the species assemblage and habitat use of cetaceans in the Svalbard Archipelago, based on observations from 2002 to 2014. *Polar Research*, *37*(1), 1463065. https://doi.org/10.1080/17518369.2018.1463065

Teigen, S. H., Nilsen, F., & Gjevik, B. (2010). Barotropic instability in the West Spitsbergen Current. *Journal of Geophysical Research*, *115*, C07016. https://doi.org/10.1029/2009JC005996

Teigen, S. H., Nilsen, F., Skogseth, R., Gjevik, B., & Beszczynska-Möller, A. (2011). Baroclinic instability in the West Spitsbergen Current. *Journal of Geophysical Research*, *116*, C07012. https://doi.org/10.1029/2011JC006974

Thomson, R., & Emery, W. (2001). *Data analysis methods in physical oceanography*. Heidelberg: Elsevier.

Vaage, K., Pickart, R. S., Pavlov, V., Lin, P., Torres, D. J., Ingvaldsen, R., et al. (2016). The Atlantic water boundary current in the Nansen Basin: Transport and mechanisms of lateral exchange. *Journal of Geophysical Research: Oceans*, *121*, 6946–6960. https://doi.org/10.1002/2016JC011715

Vennell, R., & Beatson, R. (2006). Moving vessel acoustic Doppler current profiler measurement of tidal stream function using radial basis functions. *Journal of Geophysical Research*, *111*, C09002. https://doi.org/10.1029/2005JC003321

Vennell, R., & Beatson, R. (2009). A divergence-free spatial interpolator for large sparse velocity data sets. *Journal of Geophysical Research*, *114*, C10024. https://doi.org/10.1029/2008JC004973

Visbeck, M. (2002). Deep velocity profiling using lowered acoustic Doppler current profilers: Bottom track and inverse solutions. *Journal of Atmospheric and Oceanic Technology*, *19*(5), 794–807. https://doi.org/10.1175/1520-0426(2002)019<0794:DVPULA>2.0.CO;2

von Appen, W.-J., Schauer, U., Hattermann, T., & Beszczynska-Möller, A. (2016). Seasonal cycle of mesoscale instability of the West Spitsbergen Current. *Journal of Physical Oceanography*, *46*, 1231–1254. https://doi.org/10.1175/JPO-D-15-0184.1

Walczowski, W., Piechura, J., Osinski, R., & Wieczorek, P. (2005). The West Spitsbergen Current volume and heat transport from synoptic observations in summer. *Deep-Sea Research Part I: Oceanographic Research Papers*, *52*(8), 1374–1391. https://doi.org/10.1016/j.dsr.2005.03.009

Wassmann, P., Kosobokova, K. N., Slagstad, D., Drinkwater, K. F., Hopcroft, R. R., Moore, S. E., et al. (2015). The contiguous domains of Arctic Ocean advection: Trails of life and death. *Progress in Oceanography*, *139*, 42–65. https://doi.org/10.1016/j.pocean.2015.06.011

Wekerle, C., Wang, Q., von Appen, W.-J., Danilov, S., Schourup-Kristensen, V., & Jung, T. (2017). Eddy-resolving simulation of the Atlantic water circulation in the Fram Strait with focus on the seasonal cycle. *Journal of Geophysical Research: Oceans*, *122*, 8385–8405. https://doi.org/10.1002/2017JC012974

Erratum

In the originally published version of this article, the survey name given in the third row of Table 1 was incorrectly given as IMR survey S2014618. The correct survey name is UNIS AGF214 survey HM2014618; the error did not impact the scientific content of the paper, and has now been corrected. This may be considered the official version of record.